A Functional Architecture for Scalable Quantum Computing

Eyob A. Sete, William J. Zeng, Chad T. Rigetti

Rigetti Computing

Berkeley, California

Email: {eyob,will,chad}@rigetti.com

Abstract—**Quantum computing devices based on superconducting quantum circuits have rapidly developed in the last few years. The building blocks—superconducting qubits, quantum-limited amplifiers, and two-qubit gates—have been demonstrated by several groups. Small prototype quantum processor systems have been implemented with performance adequate to demonstrate quantum chemistry simulations, optimization algorithms, and enable experimental tests of quantum error correction schemes. A major bottleneck in the effort to devleop larger systems is the need for a scalable functional architecture that combines all thee core building blocks in a single, scalable technology. We describe such a functional architecture, based on a planar lattice of transmon and fluxonium qubits, parametric amplifiers, and a novel fast DC controlled two-qubit gate.**

Keywords—*quantum computing, superconducting integrated circuits, computer architecture.*

I. INTRODUCTION

The underlying hardware for quantum computing has advanced to make the design of the first scalable quantum computers possible. Superconducting chips with 4–9 qubits have been demonstrated with the performance required to run quantum simulation algorithms [1]–[3], quantum machine learning [4], and quantum error correction benchmarks [5]–[7].

These new hardware demonstrations have been matched with advances in applications for relatively small and noisy quantum computing systems. Quantum-classical hybrid algorithms—including variational quantum eigensolvers [8]–[10], correlated material simulations [11], and approximate optimization [12]—have much promise in reducing the overhead required for valuable applications. In machine learning and quantum simulation, particularly for catalysts [13] and high temperature superconductivity [9], scalable quantum computers promise performance unrivaled by classical supercomputers.

A. Superconducting Qubits

Unlike conventional integrated circuits, a quantum integrated circuit requires ultra-low dissipation and ultra-low noise operation. Superconducting qubits with cryogenic operation and superconducting materials, meet these requirements. The non-dissipative nature of these circuits allows electric signals to be carried without energy loss, preserving quantum coherence. Information is stored in non-linear resonators, where the presence or absence of a photon at the resonant qubit frequency ω_{01} encodes the $|1\rangle$ or $|0\rangle$ state of the qubit. The technology requires that the energy of the thermal fluctuations
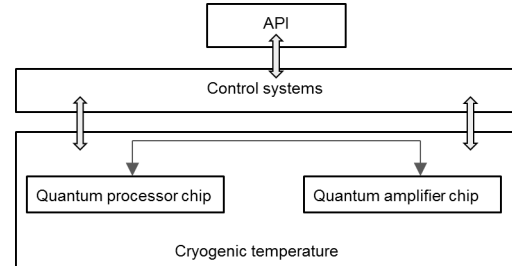

Fig. 1. A schematic of a functional layout of a quantum computing system.

$k_B T$ should be much less than the energy of the photon at the qubit transition energy $\hbar\omega_{01}$. In a large system where superconducting circuits are packed together, unwanted crosstalk among devices is inevitable. To reduce or minimize crosstalk, efficient packaging and isolation of individual devices is imperative and substantially improves the performance of the system.

Superconducting qubits are made using Josephson tunnel junctions which are formed by two superconducting thin electrodes separated by a dielectric material. The dielectric material is thin enough (a few nm) to allow tunneling of discrete charges (Cooper pairs) through the insulating barrier.

One of the requirements of gate-based quantum computer is a universal set of quantum gates. Although it is possible to generate these gates using microwave signals applied to the circuits, controllability and scalability remains a challenge. One can instead generate the single qubit gates via microwaves and two qubit gates using DC controlled frequency tunable qubits. In the architecture proposed here, fixed frequency transmon qubits and frequency tunable fluxonium qubits are used. On one hand, transmons are easy to design and are robust to charge noise, thus yielding improved coherence time [14]. On the other hand, fluxonium qubits are also designed to be insensitive to charge noise and have wide frequency tunablity with strong nonlinearity [15]. In particular, strong nonlinearity of the fluxonium along with DC tunability allows us to generate fast high fidelity two qubit gates.

B. Quantum limited amplifiers

Quantum limited amplifier is an essential component of a scalable quantum computing system. It allows fast high-fidelity single-shot readout of qubits. Each qubit is measured using the method of dispersive readout, where the qubit is weakly coupled to a superconducting linear resonator. This weak coupling imparts a qubit-state dependent resonator frequency shift,

which appears as a phase shift in a reflected or transmitted microwave signal. By measuring this signal via the homodyne method, we can infer the state of the qubit.

Quantum limited amplifiers [16]–[18] such as Josephson parametric amplifier, Josephson bifurcation amplifier, and Josephson parametric converter are nonlinear superconducting resonators made of Josephson junctions and thus operates at cryogenic temperature. Quantum limited amplifiers are designed by exploiting nondissipative and nonlinear properties of Josephson junction at very low temperature. These devices are characterized by amplifier bandwidth, gain and dynamic range.

In a scalable quantum computing system, integration of quantum limited amplifiers on a chip is needed. Depending on the bandwidth of these amplifiers each qubit readout can have a dedicated amplifier or multiple qubits can be read out by a single broadband amplifier. Figure 1 illustrates an example setup of a quantum computing system.

II. FUNCTIONAL ARCHITECTURE

We propose a functional architecture of coupled fluxonium and transmon qubits. Fixed-frequency transmon qubits are placed at the vertices of a square lattice, while fluxonium qubits are placed at on the edges. The parking frequency of each fluxonium is chosen to be between the frequencies of its two neighboring transmons, so that we label one as the *lower transmon* and the other as the *upper transmon* respectively. An example 40-qubit segment of this architecture, comprising 16 transmons and 24 fluxoniums is illustrated in Figure 2. Equivalently, the architecture is a bi-partite graph of transmon and fluxonium qubits, where edges are one of two colors.

On each transmon or fluxonium qubit the single-qubit rotation gates $R_X(\theta) = \exp[-i\frac{\theta}{2}X]$ and $R_Y(\theta) = \exp[-i\frac{\theta}{2}Y]$ form a parametrized class of primitive gates, where X and Y are the usual Pauli matrices. The rotation angle θ may be implemented to high enough accuracy that gates are decoherence limited, i.e., it suffices to consider θ as exactly accurate, but with a limited gate fidelity due to finite qubit lifetimes. In practice a limited set of gates from this class are chosen for tune-up, e.g., $\theta \in \{\pm\pi, \pm\pi/2, \pm\pi/4, \pm\pi/8, \pm\pi/16, \pm\pi/32\}$.

In addition to being a qubit itself, the fluxonium qubits act as tunable couplers, enabling two classes of two-qubit gates between the transmons and fluxoniums. The first class, called SWAP class, allows gates from the set $\{\text{iSWAP}, \sqrt{\text{iSWAP}}, \text{iSWAP}^{1/4}, \ldots\}$, and can be applied between any fluxonium and transmon pair. A second two-qubit gate class (called CPhase class) is available between a fluxonium and an upper transmon. This is a parametrized class of the four controlled phase gate types $\{C_{00}(\phi), C_{01}(\phi), C_{10}(\phi), C_{11}(\phi)\}$, where C_{ij} performs a phase shift of ϕ on input of the two qubit state $|ij\rangle$.

The CPhase class and SWAP class two-qubit gate primitives, along with single qubit rotations on the transmons and fluxoniums, enable universal quantum computation. Other two-qubit gates, such as the controlled-not can be synthesized from these primitives [19]. We describe these two qubit gates in more detail in the following Section.
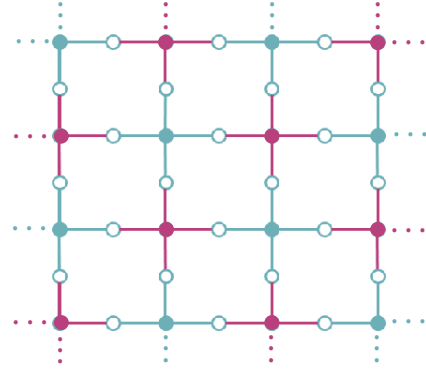

Fig. 2. Solid blue circles are lower transmon qubits and solid red circles are upper transmon qubits. Empty circles are fluxonium qubits. Qubit couplings are indicated by the edges and allow two different sets of natural two-qubit gates, as described in the text. Blue edges indicate a coupling between a fluxonium and a lower transmon, allowing two-qubit gates from of the SWAP class. Red edges indicate a coupling between a fluxonium and an upper transmon, allowing CPhase class gates

III. THEORY OF TWO-QUBIT GATES

A. The transmon-fluxonium SWAP class gate

Transmon and fluxonium qubits are coupled capacitively. Treating both fluxonium and transmon qubits as having arbitrary energy-level systems, the Hamiltonian can be described as ($\hbar = 1$)

$$H = \sum_j \omega_j^{\mathrm{T}}|j\rangle\langle j| + \sum_m \omega_m^{\mathrm{F}}(t)|m\rangle\langle m| + \sum_{ijkm} g_{ij,km}|i\rangle\langle j| \otimes |k\rangle\langle m|, \quad (1)$$

where ω_j^{T} is the frequency jth energy level of the transmon and $\omega_m^{\mathrm{F}}(t)$ is the frequency of the mth level of fluxonium which is tunable in time; $g_{ij,km}$ is the coupling between the $|i\rangle \to |j\rangle$ transition of transmon and the $|k\rangle \to |m\rangle$ transition of fluxonium. Fluxnoium qubit energy levels have a strong non-linearity, and so this qubit can be accurately modeled by a two-level system. As the transmon is relatively linear, we include at least the $|2\rangle$ in our model. In view of this, the Hamiltonian of the coupled system reduces to

$$H = \begin{pmatrix} 0 & 0 & 0 \\ 0 & \omega_{01}^{\mathrm{T}} & 0 \\ 0 & 0 & \omega_{01}^{\mathrm{T}} + \omega_{12}^{\mathrm{T}} \end{pmatrix} \otimes I^{(2)} \quad (2)$$

$$+ \frac{1}{2}\omega_{01}^{\mathrm{F}}(t)I^{(1)} \otimes \sigma_{2z} + g(\sigma_1\sigma_2^\dagger + \sigma_1^\dagger\sigma_2 + \sigma_1^\dagger\sigma_2^\dagger + \sigma_1\sigma_2),$$

where ω_{01}^{T} and $\omega_{12}^{\mathrm{T}} = \omega_{01}^{\mathrm{T}} - \eta^{\mathrm{T}}$ are the $|0\rangle \to |1\rangle$ and $|1\rangle \to |2\rangle$ transition frequencies of the transmon, with η^{T} being the anharmonicity of the transmon, and $\omega_{01}^{\mathrm{F}}(t)$ is the $|0\rangle \to |1\rangle$ transition frequency of the fluxonium; g is the coupling strength between the $|0\rangle \to |1\rangle$ transition of the transmon and the fluxonium. Here $I^{(1)}$ and $I^{(2)}$ are 3×3 and 2×2 identity matrices respectively, and the lowering operators of the qubits are given by

$$\sigma_1 = \begin{pmatrix} 0 & 1 & 0 \\ 0 & 0 & \sqrt{2} \\ 0 & 0 & 0 \end{pmatrix} \otimes I^{(1)}, \quad \sigma_2 = I^{(1)} \otimes \begin{pmatrix} 0 & 0 \\ 1 & 0 \end{pmatrix}. \quad (3)$$

Instead of directly tuning the coupling strength we are tune the fluxonium frequency to control the coupling between the two qubits.
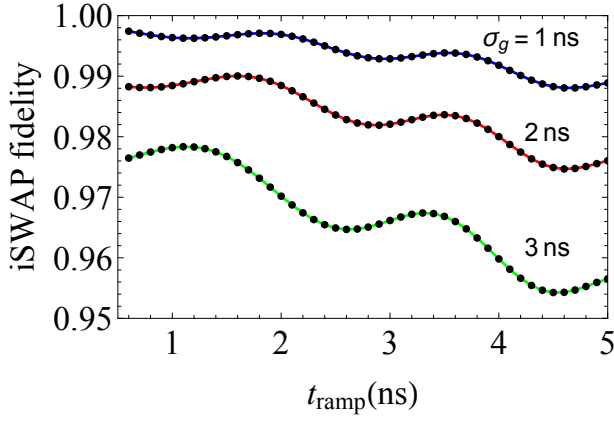
Fig. 3. iSWAP gate fidelity versus the ramp up and down time of the fluxnium frequency pulse for different values of the pulse ramp up or down slope. Here we used transmon frequencies are $\omega_{01}^{\mathrm{T}}/2\pi = 4.1$ GHz and $\omega_{12}^{\mathrm{T}}/2\pi = 3.87$ GHz, fluxonium is park frequency $\omega_{\mathrm{p}}/2\pi = 4.7$ GHz and coupling strength $g/2\pi = 2.5$ MHz.

For the frequencies of interest (4–8 GHz), the coupling strength is much smaller than the the transition frequencies, $g \ll \omega_1, \omega_2$. This justifies the use of the rotating wave approximation in (2), where we drop the counter rotating terms $\sigma_1\sigma_2$ and $\sigma_1^\dagger\sigma_2^\dagger$. Thus, the total Hamiltonian now has the form

$$H = \begin{pmatrix} 0 & 0 & 0 \\ 0 & \omega_{01}^{\mathrm{T}} & 0 \\ 0 & 0 & \omega_{01}^{\mathrm{T}} + \omega_{12}^{\mathrm{T}} \end{pmatrix} \otimes I^{(2)} \qquad (4)$$
$$+ \frac{1}{2}\omega_{01}^{\mathrm{F}}(t)I^{(1)} \otimes \sigma_{2z} + g(\sigma_1\sigma_2^\dagger + \sigma_1^\dagger\sigma_2).$$

The two qubits are initially detuned so that there is no interaction between them. We then tune the frequency of the fluxonium towards the frequency of the transmon to achieve a resonant coupling described by the interaction part of the Hamiltonian $H_{\mathrm{int}} = g(\sigma_1\sigma_2^\dagger + \sigma_1^\dagger\sigma_2)$. This qubit-qubit interaction generates the SWAP two-qubit gate class. In particular, for resonance interaction time $t_s = \pi/2g$, we apply an iSWAP gate between the transmon and fluxonium qubits

$$\text{iSWAP} = e^{-iH_{\mathrm{int}}t_s} = \exp[-iH_{\mathrm{int}}\pi/2g]. \qquad (5)$$

The total gate time will be the iSWAP time plus the ramp up and down time: $t_{\mathrm{iSWAP}} = t_s + t_{\mathrm{ramp}}$. In general, for an arbitrary iSWAP exponent gate, the gate time can be written as

$$t_{\sqrt[n]{\text{iSWAP}}} = \frac{\pi}{2ng} + t_{\mathrm{ramp}}, \qquad (6)$$

where $n = 1, 2, 4, \ldots$. As an example, we consider a transmon with frequency $\omega_1/2\pi = 4.1$ GHz, coupling strength $g/2\pi = 2.5$ MHz, fluxonium parking frequency $\omega_{\mathrm{p}}/2\pi = 4.7$ GHz with a bias pulse shape

$$\omega_{01}^{\mathrm{F}}(t) = \omega_{\mathrm{p}} + \frac{\omega_1 - \omega_{\mathrm{p}}}{2}\left[\mathrm{Erf}\left(\frac{t - t_{\mathrm{ramp}}}{\sqrt{2}\sigma_g}\right) - \mathrm{Erf}\left(\frac{t - t_s}{\sqrt{2}\sigma_g}\right)\right], \qquad (7)$$

where σ_g is the slope of the ramp up and down part of the pulse. Figure 3 shows the fidelity versus t_{ramp} for the above set of parameters and for $\sigma_g = 1$ ns. At $t_{\mathrm{ramp}} = 2$ ns, the iSWAP gate fidelity is 99.69% with a total gate time $t_{\mathrm{iSWAP}} = 102$ ns. Here we used $T_1 = 10\mu s$ for both qubits. The fidelity is limited
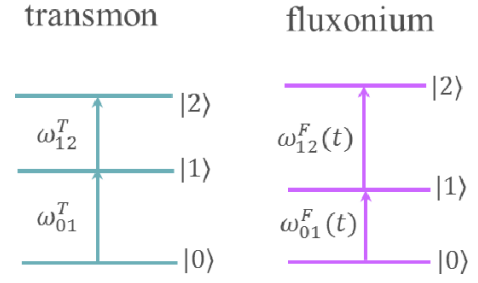

Fig. 4. Energy level diagrams of an upper transmon ($\omega_{01}^{\mathrm{F}} > \omega_{01}^{\mathrm{T}}$) and a fluxonium qubit.

by how fast the pulse ramps up or down. The faster fluxonium frequency approaches the transmon frequency (small σ_g), the higher the fidelity and vice versa.

B. The transmon-fluxonium CPhase class gate

The second class of two-qubit gates that can be generated between a transmon and fluxonium qubit is the controlled-phase (CPhase) class. These gates can be realized using level $|2\rangle$ of the transmon qubit and works when the fluxonium qubit $|0\rangle \rightarrow |1\rangle$ transition is lower than the transmon $|0\rangle \rightarrow |1\rangle$ transition [19]–[22]. The relevant qubit energy level diagram is shown in Figure 4.

The Hamiltonian (in the rotating wave approximation) is given by

$$H = \begin{pmatrix} 0 & 0 & 0 \\ 0 & \omega_{01}^{\mathrm{T}} & 0 \\ 0 & 0 & \omega_{01}^{\mathrm{T}} + \omega_{12}^{\mathrm{T}} \end{pmatrix} \otimes I^{(2)} \qquad (8)$$
$$+ I^{(1)} \otimes \begin{pmatrix} 0 & 0 & 0 \\ 0 & \omega_{01}^{\mathrm{F}} & 0 \\ 0 & 0 & \omega_{01}^{\mathrm{F}}(t) + \omega_{12}^{\mathrm{F}}(t) \end{pmatrix} + g(\sigma_1\sigma_2^\dagger + \sigma_1^\dagger\sigma_2),$$

where ω_{01}^{T} and $\omega_{12}^{\mathrm{T}} = \omega_{01}^{\mathrm{T}} - \eta^{\mathrm{T}}$ are the $|0\rangle \rightarrow |1\rangle$ and the $|1\rangle \rightarrow |2\rangle$ transition frequencies of the transmon with η^{T} being the anharmonicity of the transmon, $\omega_{01}^{\mathrm{F}}(t)$ and $\omega_{12}^{\mathrm{F}}(t)$ the $|0\rangle \rightarrow |1\rangle$ and $|1\rangle \rightarrow |2\rangle$ transition frequencies of the fluxonium. Here g is the fluxonium-transmon coupling strength, and

$$\sigma_1 = \begin{pmatrix} 0 & 1 & 0 \\ 0 & 0 & \sqrt{2} \\ 0 & 0 & 0 \end{pmatrix} \otimes I^{(2)}, \sigma_2 = I^{(1)} \otimes \begin{pmatrix} 0 & 1 & 0 \\ 0 & 0 & \sqrt{2} \\ 0 & 0 & 0 \end{pmatrix}. \qquad (9)$$

To generate the CPhase gate, we tune the fluxonium from its parking frequency to the $|1\rangle \rightarrow |2\rangle$ transition frequency ω_{12}^{T} of transmon. After some interaction time, determined by the coupling, we tune the frequency of the fluxonium back to its parking frequency, see Figure 5. During this interaction time, the states of the two qubits hybridize and the resulting eigenstates repel each other, giving rise to the phase shifts that implement the gate. We are interested in the repulsion between the eigenstates corresponding to composite state $|11\rangle$ and $|20\rangle$. (Here the first digit represents transmon energy levels and the second digit represents the fluxonium energy levels.)

When the frequency of the fluxonium is tuned towards ω_{12}^{T}, the $|11\rangle$ and $|20\rangle$ energy levels repel each other resulting in a phase shift in level $|11\rangle$ as well as $|20\rangle$. Since the computational gate is defined in the basis $\{|00\rangle, |01\rangle, |10\rangle, |11\rangle\}$,
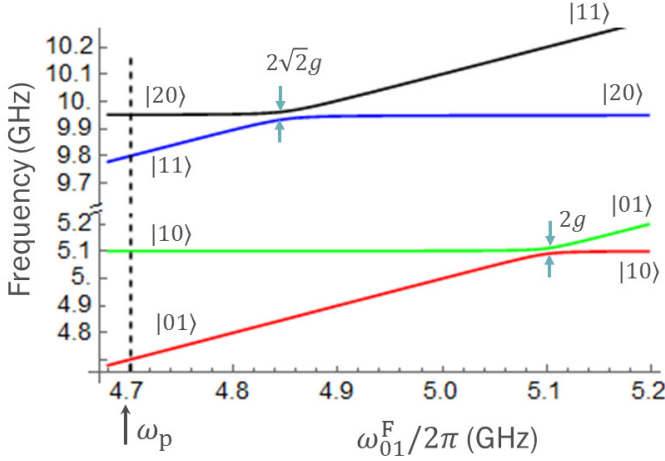
Fig. 5. Eigenfrequencies of the transmon-fluxonium coupled system showing avoided crossing between different transitions. Sufficient level repulsion between $|11\rangle$ and $|20\rangle$ gives the needed phase shift for the state $|11\rangle$ that defines the controlled phase gate. The vertical dashed line shows the parking frequency at $\omega_p/2\pi =4.7$ GHz.
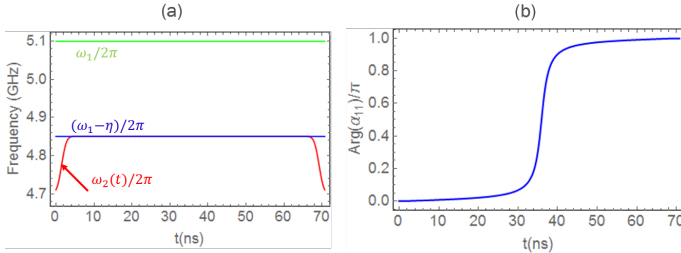

Fig. 6. (a) Bare (uncoupled) fluxonium frequency pulse and transmon frequencies (b) Accumulated phase by the state $|11\rangle$ as a function of time.

the phase shift acquired by $|20\rangle$ does not affect the gate fidelity. This tuning of fluxonium also affects the states $|10\rangle$ and $|01\rangle$, creating some phase shift. This effect is usually very small because it occurs at a frequency far away from the frequency at which $|11\rangle$ and $|20\rangle$ repulsion happens, ω_{12}^T. Note that the difference between the two frequencies at which the repulsion occurs is in fact the transmon anharmonicity η^T. The higher the anharmonicity the lower the leakage to these levels, the better the gate fidelity.

In principle, the repulsion between $|11\rangle$ and $|02\rangle$ can affect the phase shift acquired by $|11\rangle$ and thus the gate fidelity. Note that the avoided crossing between $|11\rangle$ and $|02\rangle$ occurs a few GHz away from that of the $|11\rangle$ and $|20\rangle$ states due to strong fluxonium anharmonicity. This means that the contribution to the phase shift of $|11\rangle$ due to repulsion from level $|02\rangle$ is negligible. The phase shift that $|11\rangle$ state acquires is given by

$$\phi = \int_0^{t_{CPhase}} \sqrt{2}g\,dt = \sqrt{2}gt_{CPhase}. \qquad (10)$$

The CPhase$_{11}$ (or controlled-Z) gate can be realized by choosing the phase $\phi = \pi$ with a gate time

$$t_{CPhase} = \pi/\sqrt{2}g. \qquad (11)$$

Using a flat-top waveform for the fluxonium qubit tuning,

$$\omega_{01}^F(t) = \omega_p + \frac{\omega_{12}^T - \omega_p}{2}\left[\mathrm{Erf}\left(\frac{t - t_{ramp}}{\sqrt{2}\sigma_g}\right) - \mathrm{Erf}\left(\frac{t - t_{CPhase}}{\sqrt{2}\sigma_g}\right)\right],$$

we numerically simulate the gate fidelity assuming the transmon frequency $\omega_{01}^T/2\pi = 5.1$ GHz, and qubit anharmonicity $\eta^T/2\pi = 250$ MHz, coupling strength $g/2\pi = 5$ MHz, and fluxonium qubit park frequency $\omega_p/2\pi = 4.7$ GHz, pulse ramp width $\sigma_g = 1$ ns, and ramp time $t_{ramp} = 4\sqrt{2}\sigma_g$. In Figure 6 we show the pulse shape of the fluxonium qubit and the phase accumulated by $|11\rangle$ state. For these parameters, the CPhase gate fidelity is 99.97% with a gate time $t_{CPhase} = \pi/\sqrt{2}g = 70.7$ ns.

IV. CONCLUSION

In this work we present a novel functional architecture for superconducting quantum computing. This architecture can be tiled in the plane, is universal, and offers high performance two-qubit gates. An implementation of this functional architecture with mid-range qubit performance of relaxation times (T_1) of 5–20 μs and dephasing times (T_2) of 10–30 μs across the chip would offer a valuable resources for studying quantum algorithms and benchmarks. We introduce a reasonable performance parameter for a quantum processor called the *total quantum factor* (TQF) given by:

$$\mathrm{TQF} := \frac{T_1}{t_g} \times n_q,$$

where T_1 is the average coherence time of all the qubits on the chip, t_g is the longest gate time in the qubits universal set, and n_q is the number of qubits. Gate times of 50 ns for single qubit gates and 102 ns for the SWAP class gates in the 40-qubit example from Figure 2, with an average $T_1 = 10\mu$s, and two-qubit fidelity of 99.69% would result in a TQF of 3921.

From an algorithmic perspective, TQF gives a rough estimates of the size of the quantum circuit (circuit width times circuit depth) that can be run before the processor's performance decoheres. Recent demonstrations have shown that a TQF of a few hundred is sufficient to run scalable quantum simulations of electronic structure problems for very small molecules [1]. Future work on simulating quantum algorithms under real noise parameters will allow for more accurate estimates of required TQF to run larger problem instances.

In addition to the ability to run optimization and simulation algorithms, the functional architecture presented here also allows for benchmark tests of quantum error correction. Specifically, the transmon qubits can be considered data qubits in a surface code quantum computing architecture [23], [24]. In this implementation, the fluxonium qubits act as ancillas that implement parity measurements on the faces of the square lattice formed by the transmon qubits.

In conclusion, reliable hardware building blocks and promising near term algorithms have incentivized the design of a new functional architecture for quantum computing. Future implementations and improvements in this design unlock a scalable platform for testing, optimizing, and developing quantum algorithms.

References

[1] P. O'Malley, R. Babbush, I. Kivlichan, J. Romero, J. McClean, R. Barends, J. Kelly, P. Roushan, A. Tranter, N. Ding *et al.*, "Scalable quantum simulation of molecular energies," *arXiv preprint arXiv:1512.06860*, 2015.

[2] M. R. Geller, J. M. Martinis, A. T. Sornborger, P. C. Stancil, E. J. Pritchett, H. You, and A. Galiautdinov, "Universal quantum simulation with prethreshold superconducting qubits: Single-excitation subspace method," *arXiv preprint arXiv:1505.04990*, 2015.

[3] R. Barends, A. Shabani, L. Lamata, J. Kelly, A. Mezzacapo, U. L. Heras, R. Babbush, A. Fowler, B. Campbell, Y. Chen *et al.*, "Digitized adiabatic quantum computing with a superconducting circuit," *arXiv preprint arXiv:1511.03316*, 2015.

[4] D. Riste, M. P. da Silva, C. A. Ryan, A. W. Cross, J. A. Smolin, J. M. Gambetta, J. M. Chow, and B. R. Johnson, "Demonstration of quantum advantage in machine learning," *arXiv preprint arXiv:1512.06069*, 2015.

[5] J. M. Chow, S. J. Srinivasan, E. Magesan, A. Córcoles, D. W. Abraham, J. M. Gambetta, and M. Steffen, "Characterizing a four-qubit planar lattice for arbitrary error detection," in *SPIE Sensing Technology+ Applications*. International Society for Optics and Photonics, 2015, pp. 95 001G–95 001G.

[6] J. Kelly, R. Barends, A. Fowler, A. Megrant, E. Jeffrey, T. White, D. Sank, J. Mutus, B. Campbell, Y. Chen *et al.*, "State preservation by repetitive error detection in a superconducting quantum circuit," *Nature*, vol. 519, no. 7541, pp. 66–69, 2015.

[7] D. Ristè, S. Poletto, M.-Z. Huang, A. Bruno, V. Vesterinen, O.-P. Saira, and L. DiCarlo, "Detecting bit-flip errors in a logical qubit using stabilizer measurements," *Nature communications*, vol. 6, 2015.

[8] A. Peruzzo, J. McClean, P. Shadbolt, M.-H. Yung, X.-Q. Zhou, P. J. Love, A. Aspuru-Guzik, and J. L. OBrien, "A variational eigenvalue solver on a photonic quantum processor," *Nature communications*, vol. 5, 2014.

[9] D. Wecker, M. B. Hastings, and M. Troyer, "Progress towards practical quantum variational algorithms," *Physical Review A*, vol. 92, no. 4, p. 042303, 2015.

[10] J. R. McClean, J. Romero, R. Babbush, and A. Aspuru-Guzik, "The theory of variational hybrid quantum-classical algorithms," *arXiv preprint arXiv:1509.04279*, 2015.

[11] B. Bauer, D. Wecker, A. J. Millis, M. B. Hastings, and M. Troyer, "Hybrid quantum-classical approach to correlated materials," *arXiv preprint arXiv:1510.03859*, 2015.

[12] E. Farhi, J. Goldstone, and S. Gutmann, "A quantum approximate optimization algorithm," *arXiv preprint arXiv:1411.4028*, 2014.

[13] M. Reiher, N. Wiebe, K. M. Svore, D. Wecker, and M. Troyer, "Elucidating reaction mechanisms on quantum computers," *arXiv preprint arXiv:1605.03590*, 2016.

[14] J. Koch, M. Y. Terri, J. Gambetta, A. A. Houck, D. Schuster, J. Majer, A. Blais, M. H. Devoret, S. M. Girvin, and R. J. Schoelkopf, "Charge-insensitive qubit design derived from the cooper pair box," *Physical Review A*, vol. 76, no. 4, p. 042319, 2007.

[15] V. E. Manucharyan, "Superinductance," Ph.D. dissertation, Yale University, 2012.

[16] I. Siddiqi, R. Vijay, F. Pierre, C. Wilson, M. Metcalfe, C. Rigetti, L. Frunzio, and M. Devoret, "Rf-driven josephson bifurcation amplifier for quantum measurement," *Physical review letters*, vol. 93, no. 20, p. 207002, 2004.

[17] R. Vijayaraghavan, "Josephson bifurcation amplier: Amplifying quantum signals using a dynamical bifurcation," Ph.D. dissertation, Yale University, 2008.

[18] B. Abdo, F. Schackert, M. Hatridge, C. Rigetti, and M. Devoret, "Josephson amplifier for qubit readout," *Applied Physics Letters*, vol. 99, no. 16, 2011.

[19] J. Chow, "Quantum information processing with superconducting qubits," Ph.D. dissertation, Yale University, 2010.

[20] F. W. Strauch, "Quantum logic gates for superconducting resonator qudits," *Phys. Rev. A*, vol. 84, p. 052313, Nov 2011. [Online]. Available: http://link.aps.org/doi/10.1103/PhysRevA.84.052313

[21] C. J. M. DiCarlo, L, J. M. Gambetta, L. S. Bishop, B. R. Johnson, D. I. Schuster, J. Majer, A. Blais, L. Frunzio, S. M. Girvin, and R. J. Schoelkopf, "Demonstration of two-qubit algorithms with a superconducting quantum processor," *Nature*, vol. 460, p. 240, 2009.

[22] J. Ghosh, A. Galiautdinov, Z. Zhou, A. N. Korotkov, J. M. Martinis, and M. R. Geller, "High-fidelity controlled-σ^Z gate for resonator-based superconducting quantum computers," *Phys. Rev. A*, vol. 87, p. 022309, Feb 2013.

[23] E. Dennis, A. Kitaev, A. Landahl, and J. Preskill, "Topological quantum memory," *Journal of Mathematical Physics*, vol. 43, no. 9, pp. 4452–4505, 2002.

[24] A. G. Fowler, M. Mariantoni, J. M. Martinis, and A. N. Cleland, "Surface codes: Towards practical large-scale quantum computation," *Physical Review A*, vol. 86, no. 3, p. 032324, 2012.